Applied Catalysis B: Environmental 341 (2024) 123316

Contents lists available at ScienceDirect

Applied Catalysis B: Environmental

journal homepage: www.elsevier.com/locate/apcatb

MXene dots as photocatalysts for CO_2 hydrogenation

Rubén Ramírez-Grau, María Cabrero-Antonino, Hermenegildo García *, Ana Primo **

Instituto de Tecnología Química, Consejo Superior de Investigaciones Científicas-Universitat Politècnica de València, Universitat Politècnica de València, Av. De los naranjos s/n, 46022 Valencia, Spain

ARTICLE INFO

Keywords:
Laser ablation
MXene dots
MXene as photocatalysts
Photocatalytic CO_2 hydrogenation

ABSTRACT

Four MXene dots (MDs) (Ti_3C_2, Ti_2C, V_2C and Nb_2C) have been prepared by laser ablation of the corresponding MAX phases in aqueous medium and subsequent separation by double centrifugation. These MDs were characterized by atomic force and transmission electron microscopy that show, respectively, thickness between 3 and 7.5 nm corresponding to few-layer nanoparticles and homogeneous lateral dimensions between 2.5 and 5 nm with high crystallinity. IR spectroscopy indicates that Ti_3C_2 and Ti_2C contain OH as surface terminal groups, while XPS indicates the presence of O on the surface for the four samples. MDs present the most intense absorption band in the UV region with onset below 400 nm. These samples exhibit photocatalytic activity for CO_2 hydrogenation to CO and methane, following the order Ti_3C_2>Nb_2C>Ti_2C>V_2C. Isotopic label experiments confirm CO_2 as the origin of the photo products. Most of the photoresponse derives from the UV photons, the photocatalytic activity increasing with the temperature in the range from 200 to 300 °C. These results show the possibility of tuning the composition, surface terminal groups, and other structural parameters of MXenes to produce semiconducting materials exhibiting important photocatalytic activity. Considering their versatility, flexible composition, and tunability, MXenes appear as promising 2D materials with intrinsic photoresponse to develop highly efficient photocatalysts.

1. Introduction

MXenes are 2D nanomaterials constituted by alternating one-atom thick layers of an early transition metal of the 3, 4, 5, or 6 groups of the Periodic Table (denoted as *"M"*) and a carbide, nitride or carbonitride layer (denoted as *"X"*) and have a general formula of $M_{n+1}X_n$ [1]. The external layers of MXenes are always metallic and these metals can be bound to a surface group that modulates their electronic properties. The interaction between the metal and the carbide/nitride layers has some metallic character that can result in a notable electrical conductivity depending on the nature of the surface functional groups. The high electrical conductivity and the large metal content explain why MXenes have become among the most widely studied electrocatalysts to promote hydrogen (HER) and oxygen evolution (OER) reactions as well as CO_2 reduction (CO2R) [2–4]. MXenes are also attracting increasing interest as photocatalysts, generally playing the role of co-catalysts replacing Pt and other noble metals. In most cases, an organic dye as light harvester or a photoresponsive semiconductor is required, while MXene promotes product formation [5,6].

The optical and conductive properties of MXenes can be altered in a large percentage depending on the nature of the surface groups and by selecting the appropriate composition [7]. The shift from conductive to semiconducting behavior will open the possibility of using MXenes as photocatalysts with intrinsic photo response by themselves, opening a gap between the occupied valence band and the empty conduction band [8,9]. The compositional and structural versatility of MXenes will allow band engineering to align the energy values of the valence and conduction band to the values required to promote a given chemical reaction.

In this context, we recently reported that MXene dots (MDs) prepared by liquid-phase laser ablation of the corresponding MAX phase exhibit intrinsic photocatalytic hydrogen generation activity in the absence of any other photoresponsive component [10]. A decrease of the lateral size of MXenes to a few nanometers results in the operation of quantum confinement effects reflected in optical absorption and photoluminescence of MDs, these MDs exhibiting photocatalytic activity. Theoretical DFT calculations for Ti_3C_2 models indicate that the bandgap depends on the diameter of the MDs and the nature of the surface

* Correspondence to: Polytechni Universtiy of Valencia.
** Correspondence to: Spanish National Research Council.
E-mail addresses: hgarcia@upv.es (H. García), aprimoar@itq.upv.es (A. Primo).

https://doi.org/10.1016/j.apcatb.2023.123316
Received 22 July 2023; Received in revised form 14 September 2023; Accepted 18 September 2023
Available online 20 September 2023

functional groups [10].

Continuing with this line of research it is of interest to further explore the photocatalytic activity of these MDs. Specifically, it would be important to determine whether or not MDs promote photocatalytic CO_2 reduction, the efficiency of the process, and the products formed. Herein it is reported that MDs are active in the photocatalytic CO_2 reduction using H_2 as electron and proton donor.

2. Results and discussion

Four MDs, namely Ti_3C_2, Ti_2C, V_2C and Nb_2C were prepared from the corresponding Al MAX phases by 522 nm laser ablation in aqueous suspension, as previously reported [10]. The procedure has the advantage of avoiding the use of tedious recipes employing corrosive HF or fluorinated reagents, while directly rendering small MXene nanoparticles (MDs). The evolution of MDs can be easily followed by monitoring the growth of particle number in dynamic laser scattering, by measuring the optical absorption, and by emission spectroscopy. Optimization of the laser power, laser frequency, and irradiation time can result in MD generation yields concerning the initial MAX material well above 50 %. Double centrifugation of the supernatant after laser ablation at increasing speed, allows a control on the particle size of the resulting MD sample. The process is illustrated in Scheme 1.

After preparation, the four MD samples were characterized by different techniques, including AFM and transmission optical microscopy. Frontal AFM images of a wide area provide a general indication of the sample homogeneity, while measurements of the MDs on atomically flat mica surfaces allowed determination with subnanometric vertical resolution of the particle thickness. Fig. 1 shows some selected AFM frontal images and thickness measurements to illustrate sample quality, while Fig. S1 in supplementary material contains additional images of the samples. Statistical analysis of a large number of particles indicates that the thickness of the MDs under study is between 3 and 7.5 nm for the four MXenes, corresponding to few-layer MDs. Table 1 lists the corresponding average thickness values for each sample. Since, for instance, it has been reported that the thickness of a single layer Ti_3C_2 is about 1.1 [11] or 1.5 [12] nm, depending on the etching procedure, the present MD samples under study correspond to 2–3 layers for Ti_3C_2, Ti_2C, and Nb_2C. In the case of V_2C, the average thickness is significantly larger, about double that for the other three samples.

The homogeneity of the sample morphology and lateral size can be assessed by transmission electron microscopy (TEM) at various magnifications. Representative TEM images are provided also in Fig. 1, while additional images are presented in Fig. S2 of supporting information. Histograms of particle size distribution were used to determine the average lateral dimensions of the MDs that range from 2.8 ± 0.2–4.3 ± 0.2 nm. Table 1 also contains the data on the average lateral size of the MD samples under study. Importantly, high resolution TEM images show that the MDs are highly crystalline (see for instance the insert of Fig. 1f), and measurements of the lattice distance for the four MD samples agree with the values reported in the literature.

The nature of the surface terminal groups was determined by infrared spectroscopy. Note that since MD preparation was performed in an aqueous medium in the absence of fluoride anions, the presence of –OH or bridging –O– groups on the surface can be anticipated. The presence of –OH groups can be determined in IR from the appearance of a broad vibration band in the 3500–3000 cm^{-1} region (Fig. 2, a). This characteristic vibration band was recorded for Ti_3C_2 and Ti_2C, but it was much less intense for Nb_2C and absent for V_2C. Based on the observation of a vibration band at about 1050 cm^{-1} (see Fig. 2), it is proposed that the surface contains predominantly –O– groups for Nb_2C and V_2C samples.

Optical absorption spectra of the four MDs were similar, with a strong absorption band in the deep UV in the region from 200 to 300 nm, with the onset extending to longer wavelengths up to 400 nm (Fig. 2,b). Similar optical UV-Vis absorption spectra were also recorded for Ti_2C, Nb_2C and V_2C (Fig. S3). In comparison, the reported UV-Vis absorption spectra of these MXenes show a continuous neutral absorption characteristic of reflecting metallic materials. Thus, while the absence of absorption bands in the UV-Vis region is characteristic of metallic materials, the appearance of an absorption band in this spectral region is characteristic of semiconducting materials and it corresponds to the electronic excitation from the valence and the conduction bands. Since the composition of the reported MXenes and the present MDs should be the same, this spectroscopic feature indicating a bandgap opening is proposed to reflect the operation of quantum confinement effects, similarly to plasmonic metal nanoparticles. Reported theoretical calculations support that the band opening as a consequence of the very small lateral particle size of the MD nanoparticles [10].

Survey XPS analysis of the MDs under study shows the expected elements, including Al in the cases of Ti_3C_2 and Ti_2C MD, but not for Nb_2C and V_2C (Fig S4). However, analysis of the XPS Al2p in Ti-containing MDs indicates that Al correspond exclusively to Al_2O_3 appearing at a binding energy of 76.0 eV that is very different in binding energy to Al metal in the MAX phase that is 72.8 eV [13]. The presence of O indicates that this element forms the surface termination of the laser generated MDs under study. The deconvolution of the high-resolution XPS peaks for each element is in agreement with the reported data for these MXenes [14,15]. Fig. 3 and Fig. S.4 in the supporting information present the experimental XPS peak for each element and the best

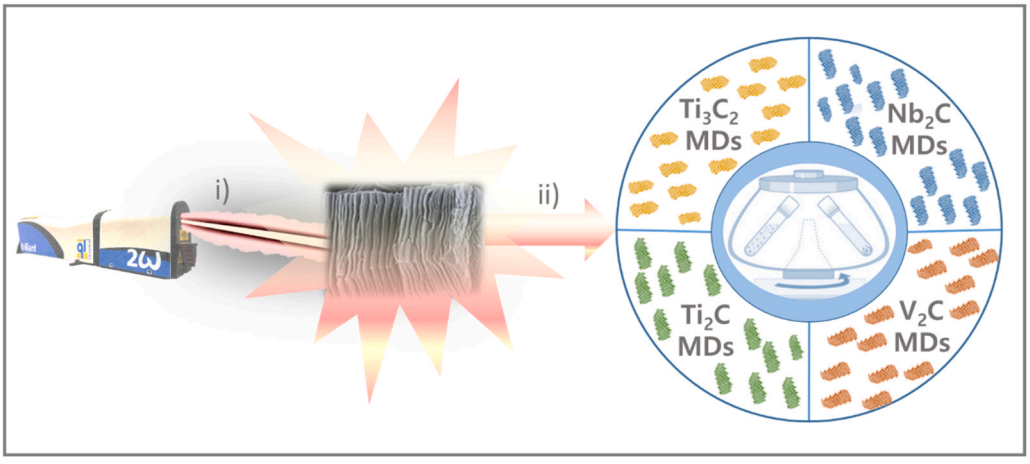

Scheme 1. A pictorial illustration of the MDs synthesis starting from the MAX phase. The steps include i) laser ablation of the MAX phase, and ii) double centrifugation to isolate the MDs. Four different MDs were prepared as indicated in the drawing.

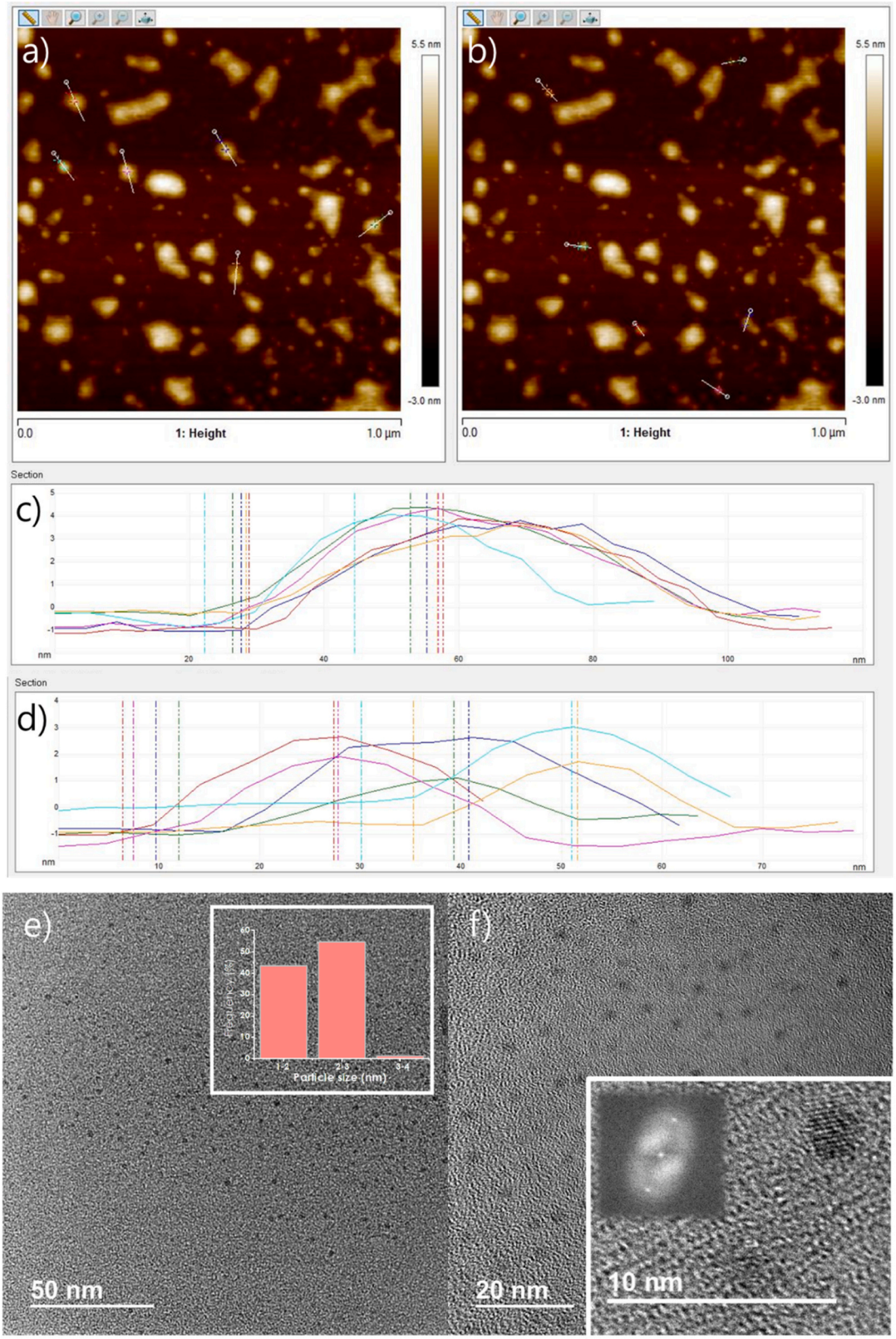

Fig. 1. AFM frontal image of Ti_3C_2 MDs in which the larger (a) and smaller (b) particles have been marked with a white line. The vertical profiles along these lines corresponding to the thickness of the various Ti_3C_2 MD particles marked in images a and b are shown in frames c and d. It can be seen in panel c that most of the particles are comprised between 4 and 5 nm, while the thickness of particles in frame d are between 3 and 4 nm; e and f) TEM images of Ti_3C_2 MDs showing their small lateral size and crystallinity. The inset of panel e) shows the histogram of the particle size distribution for 100 particles having an average dimension of 2.8 nm. The insert of image f) shows electron diffraction of the MD particle on the right hand side indicating that the particle is crystalline and 2D.

Table 1
Particle dimension data determined by AFM (thickness) and TEM (lateral size) and photocatalytic activity for the MD samples under study.

MDs composition	Average particle thickness (nm)	Average particle lateral size (nm)	CH_4 formation rate (μmol. $g^{-1}_{catalyst}h^{-1}$)	CO formation rate (μmol. $g^{-1}_{catalyst}h^{-1}$)	Selectivity CH_4/CO[a]
Ti_3C_2	3.5	2.8	140.3	100	84.9/15.1
Ti_2C	3	4.3	97.2	48	88.8/11.2
Nb_2C	3.3	3.2	140.4	82	87.2/12.8
V_2C	7.5	3.4	144.0	71	89.1/10.9

[a] Product selectivity in terms of conduction band electron consumption, i.e., 8 and 2 electrons for CH_4 and CO, respectively.

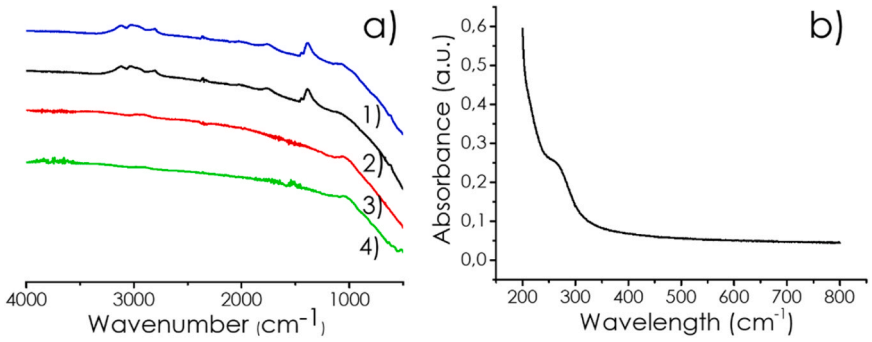

Fig. 2. a) FT-IR spectra of the samples under study 1) Ti_3C_2; 2)Ti_2C; 3) Nb_2C; 4) V_2C. b) Optical absorption spectrum of Ti_3C_2.

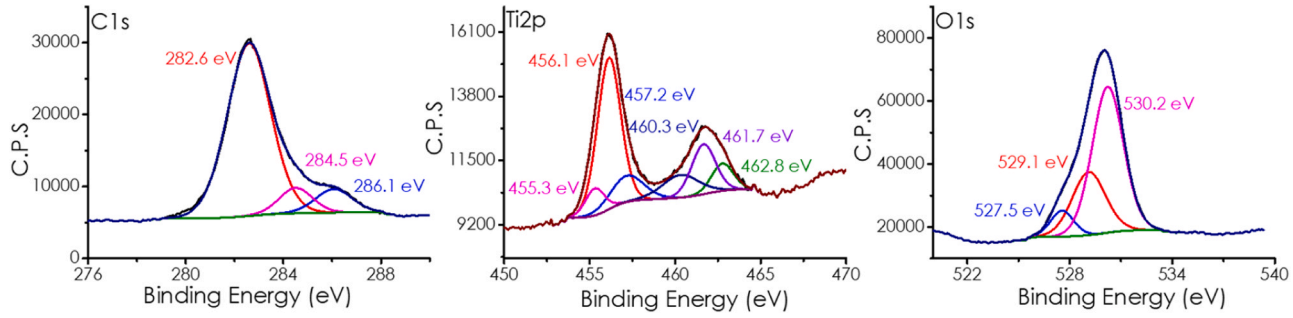

Fig. 3. High resolution XPS C1s, Ti2p, and O1s peaks of Ti_3C_2 MD, showing the best fitting to individual components and their corresponding binding energy values.

deconvolution to individual components, depending on the oxidation state and the bonding. Deconvolution of C1s peak for Ti_3C_2 MD (Fig. 3) can be fit to the contribution of three components corresponding to the major one to C bonded to the metal in MXene at about 282.6 eV, accompanied by two other contributions at 284.5 and 286.1 eV, that can be ascribed to C atoms sp2 and bonded to O, respectively. Similarly, the best fitting of the experimental high-resolution XPS O1s peak also shows three components at 527.5, 529.1, and 530.2 eV that can be assigned to O atoms connected to M atoms in three different oxidation states or chemical environments, corresponding the most intense peak to Ti bonded with OH groups. This is in agreement with the IR spectrum. In the case of Ti_3C_2, the Ti spectrum has two peaks of Ti2p1/2 and Ti2p3/3 due to spin-orbit coupling that can be deconvoluted in three main peaks with binding energy values of 455.3, 456.1, and 457.2 eV, the major one at 456.1 eV corresponding to Ti carbide.

Fig. S.5 shows the XPS analyses for Ti_2C and Nb_2C. Also in these cases, the XPS analyses were in agreement with the literature [14]. The high-resolution XPS C1s showed for both MDs three components corresponding to M-C, Csp2 and a minor contribution of C-O at binding energy values of 282.8, 284.5 and 286.5 eV, respectively. XPS O1s also showed three components for the two Ti_2C and Nb_2C dots with values of 529.0 (TiOH), 530.2 (TiO_2) and 531.3 eV (C-TiO) and 530.0 (Nb-O), 531.7 (Nb-O) and 532.4 eV (C-Nb-O), respectively. In the case of Ti_2C the high-resolution XPS Ti2p signal exhibits a doublet due to spin orbit Ti2p3/2 and Ti2p1/2 coupling that can be deconvoluted with three components at 457.3 (Ti^{3+}), 459.0 (TiO_2) and 460.5 eV (Ti^{2+}). In contrast, Nb_2C exhibits in XPS the Nb3p as a characteristic doublet due to spin-orbit coupling of a single component corresponding to C-Nb-O.

2.1. Photocatalytic activity

The activity of the four MD samples was evaluated for photocatalytic CO_2 hydrogenation under UV-Vis irradiation at 200 °C at 1.4 bar pressure, using a H_2/CO_2 ratio of 4/1. Controls in the absence of CO_2 but in the presence of MDs, under irradiation in the absence of MDs, or in the dark showed no product formation, indicating that all three components, CO_2, MDs and light are necessary in the process. These blank control experiments indicates that no products are formed in the dark, either in the presence or absence of MDs. For the four samples, the evolution of CO and methane as the only products was observed in different proportions. Fig. 4 shows the temporal product evolution upon irradiation of each MD, while Table 1 indicates the CO and methane production rates determined from these plots and their relative selectivity values considering the required electrons, 2 in the case of CO and 8 in the case of CH_4. As it can be seen in Table 1, formation of CH_4 has a selectivity above 80 % in all cases.

Isotopic labeling experiments using $^{13}CO_2$ as a reagent confirmed the origin of products by observing the formation of ^{13}CO and $^{13}CH_4$ by mass spectrometry. Fig. S.6 in supporting information presents the corresponding mass spectra of the ^{13}C labeled products.

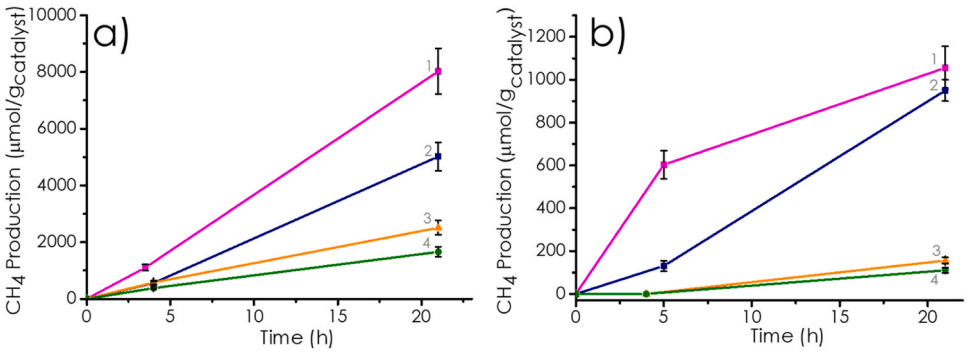

Fig. 4. Temporal profile of CH_4 evolution upon irradiation with UV-Vis (a) or visible ($\lambda > 420$ nm) (b) using as photocatalyst 1) Ti_3C_2; 2) Nb_2C; 3) V_2C; 4) Ti_2C. Irradiation conditions: gas phase, 51 mL photoreactor, 200 °C, 300 W Xe lamp, 1 mg photocatalyst, H_2/CO_2 ratio 4/1, Pressure 1.4 bar.

Photocatalytic activity depended on the nature of the MD, following the order Ti_3C_2>Nb_2C>V_2C>Ti_2C. This order is similar to that previously observed for the photocatalytic hydrogen generation in water containing sacrificial electron donors [10]. To establish the thermodynamic feasibility of the process, we initially determine experimentally the redox potential of the valence band maximum and conduction band of minimum of the MDs to know how they are aligned with the CO_2/CH_4 reduction potential. The valence band for each material was calculated by extrapolating the linear fitting of the first electron emission peak appearing in the XPS spectrum to zero intensity corrected by the work function of the instrument. Starting with this value, the conduction band was estimated by adding the value of the bandgap previously calculated from the Tauc plot (Fig. S.7). Fig. 5 presents a diagram of the calculated valence and conduction band energy values of the MDs where it is observed that the potentials of the corresponding MDs are well aligned to promote CO_2 reduction.

It was noted, however, that the reduction potential of the conduction band minimum does not determine the photocatalytic activity order, indicating that once the thermodynamic requirement is met, the reaction rate and the kinetics of the product evolution depend on the composition and the surface terminations of the MDs.

To support our proposal and the operation of a photocatalytic mechanism with the generation of photoinduced conduction band electrons and valence band holes, quenching experiments were undertaken. Thus, the presence of nitrobenzene (b.p. 210 °C) as an electron quencher in the CO_2/H_2 mixture stops completely the formation of CH_4 or CO (Fig. 6a(1)). This, can be interpreted considering that even though nitrobenzene is mostly an inert compound, it competes favorably with CO_2 for conduction band electrons, impeding the appearance of CO_2 photoproducts.

In another different experiment, photocatalytic CO_2 reduction by Ti_3C_2 was performed in the liquid phase using acetonitrile/H_2O as solvent and triethanolamine as electron donor at ambient temperature. These conditions are typical in photocatalytic CO_2 reduction implying photoinduced charge separation. Evolution of CO was again observed, even though no H_2 was present. A blank control in the absence of Ti_3C_2 did not show evidence of CO. These results can be explained by assuming that in these experiments triethanolamine is acting as an electron and proton donor, quenching photogenerated valence band holes and making possible CO_2 reduction by providing electrons and protons.

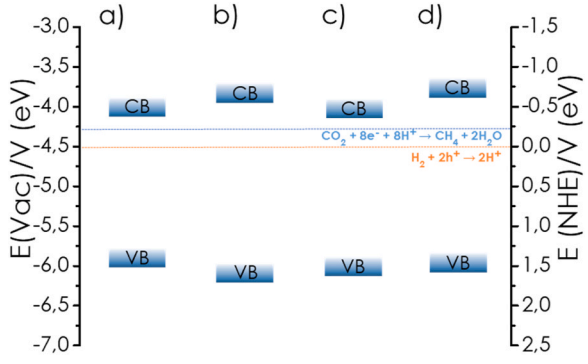

Fig. 5. Band energy diagram for a) Ti_3C_2; b) Ti_2C; c) Nb_2C; d) V_2C MDs. The standard reduction potentials of H^+/H_2 and CO_2/CH_4 have also been indicated as references.

Photocatalyst stability for Ti_3C_2 was evaluated by performing a series of consecutive runs using the same sample and following the temporal evolution. The system was evacuated after each run, but the Ti_3C_2 MD sample was not submitted to any pretreatment between the runs. A gradual decrease in the photocatalytic activity upon reuse was observed as indicated in Fig. 7a. To understand the origin of the observed activity decrease, the photocatalyst was characterized after the reaction by high resolution TEM. Fig. 7 presents representative images of the three times used Ti_3C_2 sample. As can be seen, comparing Fig. 7c (amorphous) and 7d (crystalline), it is observed the presence of amorphous regions in the used Ti_3C_2 MD sample that were not previously detected in the fresh sample. Thus, it is proposed that amorphization of the MDs, due to the stress of the photocatalytic reaction is the main reason for deactivation.

Photocatalytic CO_2 reduction has to be performed at a certain temperature to promote the process. Since frequently, the photocatalyst can catalyze the thermal CO_2 hydrogenation, it is necessary to perform the necessary controls in the dark to determine the contribution of the light assistance to the purely thermal reaction. As commented earlier, a control at 200 °C in the dark showed that no products were formed. In the present case, the influence of the reaction temperature on the photocatalytic product evolution was studied in the range from 200 to 300 °C, whereby a notable increase in CH_4 production rate was observed from 140 to 891 µmol $g^{-1}_{Ti3C2}\,h^{-1}$ (Fig. 6a). It is important to remark that control experiments at the same temperatures in the dark do not allow detecting of the formation of any product, thus, reinforcing that it is a photocatalytic reaction with no contribution of thermal catalysis in the range of temperatures indicated in Fig. 6. Therefore, in the photocatalytic reaction, the action of light makes possible to carry out CO_2 hydrogenation at temperatures much lower than those that are generally required for the pure thermal catalysis that are in the range of 500 °C and above. However, it is clear from Fig. 6 that external heat is still required when irradiation is carried out at 1 sun power. At 200 °C and using monochromatic light of 280 and 450 nm wavelength apparent quantum yields of CH_4 formation were 0.3 % and 0.043 %, respectively, while the estimated yields at 300 °C at these two wavelengths are 1.7 % and 0.23 %.

To put the photocatalytic activity of Ti_3C_2 dots into a broader context, a comparison with literature data was made. Table S1 in the supporting information summarizes photocatayltic activity data for CO_2 reduction using other photocatalysts. It should be noted that comparison

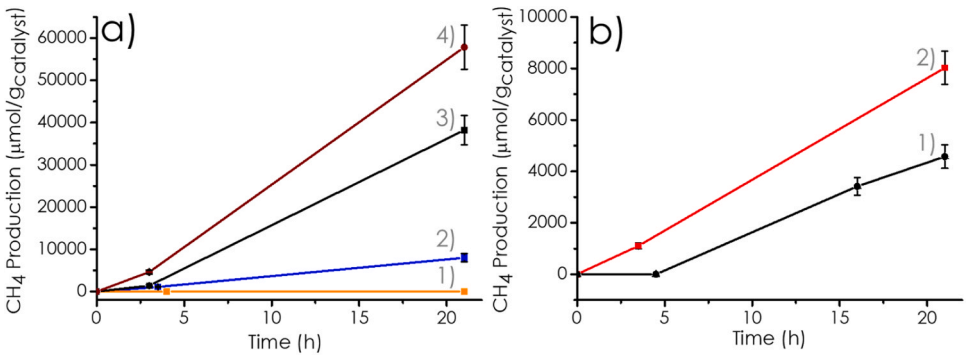

Fig. 6. a) Temporal profile of CH_4 evolution upon irradiation with UV-Vis using as photocatalyst Ti_3C_2 at different temperatures (4) 300 °C; (3) 250 °C; (2) 200 °C and (1) 200 °C upon addition of some nitrobenzene. Irradiation conditions: gas phase, 51 mL photoreactor, 300 W Xe lamp, 1 mg photocatalyst. b) Comparative of CH_4 production ($\mu mol/g_{catalyst}$) in 1) liquid phase using acetonitrile/H_2O as solvent and triethanolamine as electron donor or in 2) gas phase at 200 °C H_2/CO_2 ratio 4/1 as plot a).

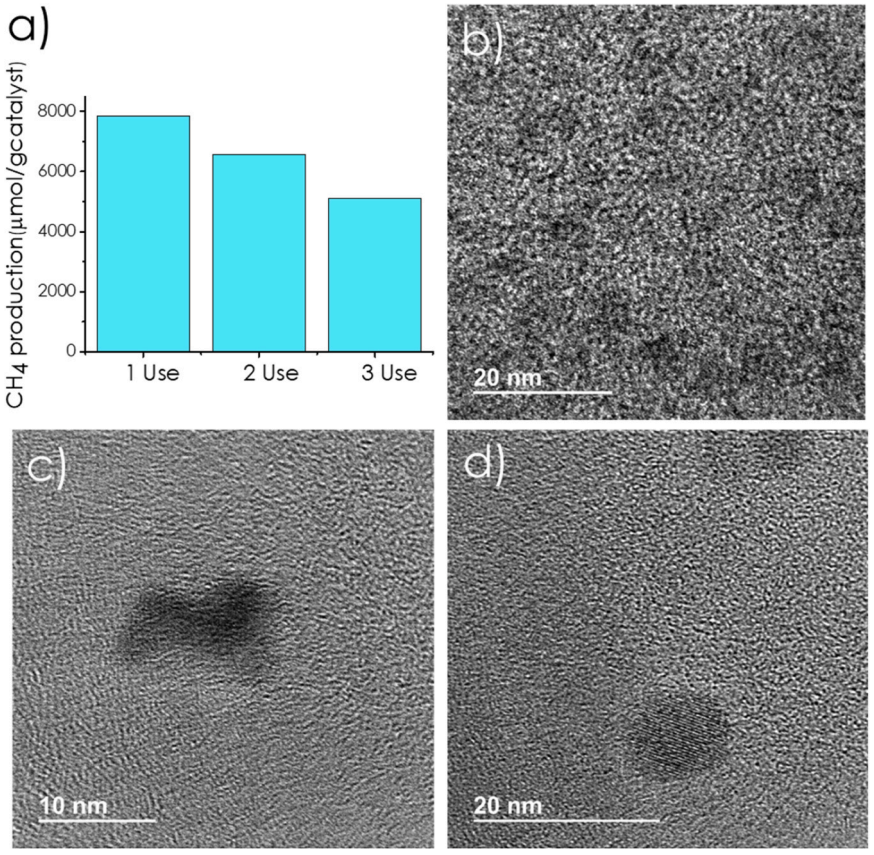

Fig. 7. a) CH_4 production rate upon consecutive use of the same Ti_3C_2 sample, showing the gradual decay in activity. Reaction condition: UV-Vis light from a 300 W Xe lamp, temperature 200 °C, photocatalyst 1 mg, time 21 h. b, c, and d) TEM images of the three-times used Ti_3C_2 sample showing the presence of amorphous (c) and crystalline particles in the used sample.

with reported data is always problematic due to the various conditions employed in the photocatalytic reaction, particularly the light spectrum and intensity. In the present case, irradiation was carried out in the gas phase with simulated sunlight at 1 sun power and heating at 300 °C. The literature has reported higher temperatures or higher light intensity. In any case, as it can be seen in Table S1, Ti_3C_2 dot compares favorably with most of the photocatalysts based on TiO_2 (entries 6–10), but the activity is lower than that of other photocatalysts used at higher temperatures (entry 1) or much higher light intensity (entry 3).

The photoresponse of MD photocatalysts was studied by using a UV cut-off filter for wavelengths shorter than 420 nm. A considerable decrease in the photocatalytic activity for the four MD samples was observed for Vis light irradiation in comparison to UV-Vis light. The results are presented in Fig. 4b. Comparison of the product evolution rate with the light of the two spectral ranges indicates that about 85 % of the photocatalytic activity derives from UV photons. This decrease in photocatalytic activity in the visible region can be easily interpreted considering that according to the UV-Vis spectra of MDs, photon absorption should occur preferentially in the UV region. The low photon absorption in the visible region of MDs explains the lower activity under visible light irradiation in comparison to the UV light. Interestingly, a change in product selectivity, particularly the absence of CO formation

was observed. These facts suggest that by the reduction potential of the respective redox pairs, CO formation should require sites of higher energy than those involved in the CH_4 formation, and activation of those sites of higher reduction potential would preferentially occur by higher energy photons.

Besides quenching experiments by nitrobenzene in the gas phase or triethanolamine in the liquid phase, further evidence in support of the occurrence of photoinduced charge separation can be achieved by metal photodeposition experiments. The formation of metal nanoparticles on the Ti_3C_2 photocatalyst can be proved by TEM analysis. Photodeposition of Pt by photogenerated conduction band electrons was performed in a deaerated aqueous medium containing methanol as a sacrificial electron donor using $KPtCl_6$ as soluble Pt salt. After 5 min irradiation with UV-Vis light, the resulting Ti_3C_2 MD sample was removed from the suspension, washed, and analyzed by TEM, whereby the presence of Pt nanoparticles on Ti_3C_2 was detected and confirmed by EDS analyses. The photogeneration of holes and their ability to promote oxidation reactions was confirmed by carrying out the photodeposition of RuO_2 from $RuCl_3$ as a soluble precursor in water and in the presence of ambient oxygen as an electron scavenger. After 5 min irradiation with the full output of the Xe lamp, the presence of RuO_2 on the Ti_3C_2 MD sample was observed by TEM and confirmed by EDS. Fig. 8 shows selected images of the Ti_3C_2 MD samples after the photodeposition experiments.

With the confirmation of the photoinduced charge separation with the generation of electrons and holes obtained by metal and metal oxide photodeposition, a plausible mechanism for photocatalytic CO_2 hydrogenation can be proposed (Scheme 2). According to this mechanism, MDs will absorb light according to their UV-Vis absorption spectrum and

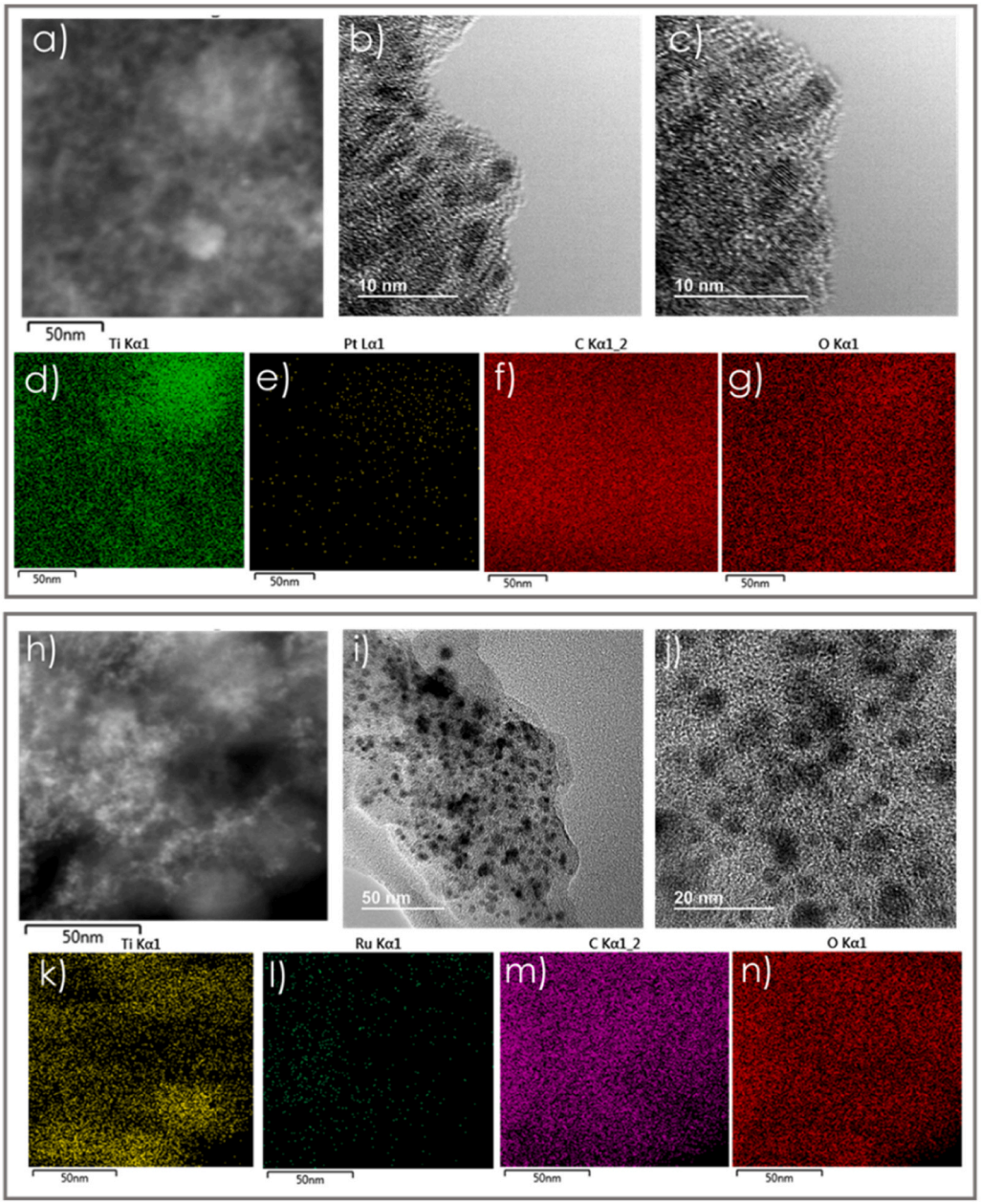

Fig. 8. a, b, and c) TEM images of Ti_3C_2 after deposition of Pt. The EDS elemental mapping showing the presence of Ti, Pt, C, and O on irradiated Ti_3C_2 sample is presented in panels d, e, f, and g, respectively. Reaction conditions: Xe lamp, N_2-purged 10^{-3} M K_2PtCl_6 solution in H_2O/EtOH in a proportion 80/20, Ti_3C_2 1 mg, 5 min irradiation at room temperature. h, i, and j) TEM images of Ti_3C_2 after deposition of RuO_2. EDS elemental mapping of Ti, Ru, C, and O for the sample after RuO_2 photodeposition is shown in frames k, l, m, and n, respectively. Reaction conditions: Xe lamp, aerated 10^{-3} M $RuCl_3$ solution in H_2O (pH 5), Ti_3C_2 1 mg, 5 min irradiation at room temperature.

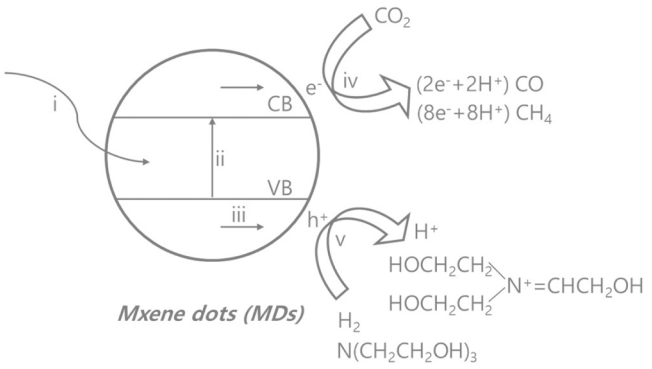

Scheme 2. Mechanistic proposal for the photocatalytic activity of MD based on the opening of a gap between the valence and the conduction band due to the small size and light absorption (*i*), photoinduced charge separation (*ii*), migration of charge carriers (*iii*) and CO_2 reduction by electrons coupled with protons (*iv*) and hole oxidation of H_2 or triethanolamine (*v*).

would undergo photoinduced charge separation with the generation of electrons and holes. Holes will oxidize H_2 to form H^+. Photogenerated electrons in the conduction band and the corresponding H^+ will reduce CO_2 to CH_4 or CO depending on the reaction conditions.

3. Conclusions

The present study has shown that MDs of few-layer thickness and small lateral size in the range of a few nanometers on their own, in the absence of a light harvester, behave as semiconductor and can promote photocatalytic CO_2 hydrogenation at moderate temperatures. This semiconducting properties contrast with the metallic character (no gap between the valence and the conduction band) of larger MXene sheets. The product formation rate increases with the temperature and a comparison with dark experiments shows that the process requires light to occur. The performance of MDs depends on their composition, Ti_3C_2 being the most active MD. Most of the photoresponse derives from the UV region that corresponds to the most intense absorption band of the MDs. Ti_3C_2 undergoes a gradual deactivation, presumably due to loss of crystallinity during the photochemical reaction, as evidenced by TEM. The interest of the present study is to show that, MXenes by themselves, can exhibit an intrinsic photocatalytic activity that can be modulated depending on the composition. Since MXenes allow a wide range of compositions, including bimetallic solid solutions and a wide range of surface functional groups, there is still much room for improvement in the intrinsic photocatalytic efficiency by adjusting these parameters and also achieving photocatalytic stability.

4. Experimental section

4.1. Material preparation

3 mg of MAX phase (Chemizone) were suspended in 3 mL of MilliQ water in a Suprasil quartz cuvette (10 ×10 mm, 3 mL vol). The suspension was submitted to ultrasounds to obtain a homogenous dispersion, capped with a rubber septum, and purged for 15 min with argon to remove oxygen from the medium. Then, the system was irradiated for 3 h using the second harmonic of a Q-switched Nd:YAG laser (Quantel Brilliant, 532 nm, 5 mJ/pulse, 5 ns fwhm) operating at 1 Hz. Finally, the resultant material was centrifuged at 4000 rpm for 4 h and, then, at 13 000 rpm for 1 h more to isolate from the bulk MAX and other phases that sediment in the process the small MXene dots (MD) that remains in the supernatant.

4.2. Photocatalytic reactions

4.2.1. Photocatalytic activity using H_2 and CO_2

The photocatalyst was placed in a quartz reactor (51 mL total volume) equipped with a flexible electrical heating ribbon and thermocouple connected to a controller that sets and keeps constant the reaction temperature at the photocatalyst bed. Then, the system was purged with H_2 for 20 min and CO_2 was introduced to obtain a H_2:CO_2 ratio of 4:1 at a total pressure of 1.4 bar. The system was heated at 200, 250 or 300 ºC Tin the dark until the temperature was stable. This was time zero of the experiments and analysis at this point does not reveal the formation of any product. Then the photocatalyst was irradiated using a Xe lamp (150 W, Hamamatsu ref. L8253; Hamamatsu spot light source L9566-04 and light guide A10014-50-0110, 1000 W m^{-2})) or with a commercially available solar simulator through a AM 1.5 G filter (Lasing ref. 81094) at one sun power. The evolution of the reaction was followed by analyzing periodically reaction aliquots in an Agilent 490 MicroGC equipped with a thermal conductivity detector and two channels, one with a MolSieve 5 A column to analyze H_2, O_2, N_2, and CO, while the other had a Pore Plot Q column to analyze the CO_2, CH_4, and short-chain hydrocarbons. Quantification was performed using calibration plots employing commercially available gas mixtures.

4.2.2. Photocatalytic activity using CH_3CN, H_2O, TEOA and CO_2

Alternatively to the previous gas-phase photocatalytic CO_2 hydrogenation, photocatalytic CO_2 reduction was also tested suspending the photocatalysis in a CH_3CN/H_2O mixture. In suspension, the photocatalytic activity for CH_4 and H_2 generation was evaluated in the presence of acetonitrile (12 mL), water (4 mL), triethanolamine (4 mL) and the corresponding amount of catalyst. The suspension was placed in a quartz reactor (51 mL) and the system was purged for 20 min under CO_2. The suspension was stirred at room temperature at 60 rpm and irradiated using a Xe lamp (150 W, Hamamatsu ref. L8253; Hamamatsu spot light source L9566–04 and light guide A10014–50–0110). The evolution of the reaction was followed by analyzing periodically reaction aliquots in an Agilent 490 MicroGC that is able to detect H_2, O_2, N_2, CO, CO_2, CH_4 among other gases.

4.3. Material characterization

The composition, oxidation state, and valance band energy of the four different MXene dots were determined by X-ray photoelectron spectra (XPS). The spectra were obtained under ultrahigh vacuum conditions with a SPECS spectrometer using a monochromatic Al (K_α = 1486.6 eV) X-ray source.

Before recording the Fourier transform infrared (FTIR) spectra of MXene dots, the sample was dried in an oven at 60 °C overnight. FTIR spectra were acquired monitoring the surface by reflectance was carried out with Bruker Tensor 27 equipment.

HRTEM images to obtain information about the morphology and size of the MXene dots were taken under an accelerating voltage of 200 kV. All the samples were prepared by drying a drop of MXene QDs suspension in a carbon-coated copper grid as a sample holder for the microscope.

The thickness of MXene dots was determined by AFM analysis with a Multimode Nanoscope 3 A instrument.

UV spectra from each material were obtained with a Cary 5000 spectrophotometer from Varian using the diffuse reflectance mode. A compressed powder was placed at the focus of an integrating sphere. Optical bandgap was determined by the Tauc plot of the diffuse reflectance optical spectrum considering the material as a direct semiconductor (n = ½). Valence band energy was determined by XPS measuring the onset energy of electrons and correcting the value for the work function of the instrument.

CRediT authorship contribution statement

Rubén Ramírez-Grau prepared and characterized the MXene dots. María Cabrero-Antonino performed the photocatalytic study. Hermenegildo García designed the Research and revised the final manuscript. Ana Primo supervised the work in the laboratory and wrote the draft.

Declaration of Competing Interest

The authors do not have any conflict of interest to declare.

Data availability

Data will be made available on request.

Acknowledgments

Financial support by the Spanish Ministry of Science and Innovation (CEX-2021-001230-S and PDI2021-0126071-OB-CO21 funded by MCIN/AEI/ 10.13039/501100011033) and Generalitat Valenciana (Prometeo 2021/038 and Advanced Materials program Graphica MFA/ 2022/023 with funding from European Union Next Generation EU PRTR-C17. I1).

Appendix A. Supporting information

Supplementary data associated with this article can be found in the online version at doi:10.1016/j.apcatb.2023.123316.

References

[1] M. Naguib, M.W. Barsoum, Y. Gogotsi, Ten years of progress in the synthesis and development of MXenes, Adv. Mater. 33 (2021), 2103393.
[2] K.S. Lakshmi, B. Vedhanarayanan, T.-W. Lin, Electrocatalytic hydrogen and oxygen evolution reactions: role of two-dimensional layered materials and their composites, Electrochim. Acta 447 (2023), 142119.
[3] T.-Y. Shuai, Z. Qi-Ni, H. Xu, C.-J. Huang, Z. Zhi-Jie, G.-R. Li, Recent advances in the synthesis and electrocatalytic application of MXene materials, Chem. Commun. 59 (2023) 3968–3999.
[4] L. Wang, M. Han, C.E. Shuck, X. Wang, Y. Gogotsi, Adjustable electrochemical properties of solid-solution MXenes, Nano Energy 88 (2021), 106308.
[5] R. Ramírez-Grau, A. Lewandowska-Andralojc, A. Primo, H. García, Accelerated transfer and separation of charge carriers during the photocatalytic production of hydrogen over Au/ZrO2–TiO2 structures by interfacial energy states, Int. J. Hydrogen Energy 48 (2023) 15956–15966.
[6] Z. Otgonbayar, W.-C. Oh, MXene-based nanocomposite for the photocatalytic CO_2 reduction: comprehensive review, Mol. Catal. 541 (2023), 113085.
[7] M. Han, K. Maleski, C.E. Shuck, Y. Yang, J.T. Glazar, A.C. Foucher, K. Hantanasirisakul, A. Sarycheva, N.C. Frey, S.J. May, Tailoring electronic and optical properties of MXenes through forming solid solutions, J. Am. Chem. Soc. 142 (2020) 19110–19118.
[8] X.-H. Zha, Q. Huang, J. He, H. He, J. Zhai, J.S. Francisco, S. Du, The thermal and electrical properties of the promising semiconductor MXene Hf2CO2, Sci. Rep. 6 (2016) 27971.
[9] J.L. Hart, K. Hantanasirisakul, A.C. Lang, B. Anasori, D. Pinto, Y. Pivak, J.T. van Omme, S.J. May, Y. Gogotsi, M.L. Taheri, Control of MXenes' electronic properties through termination and intercalation, Nat. Commun. 10 (2019) 522.
[10] R. Ramírez, A. Melillo, S. Osella, A.M. Asiri, H. Garcia, A. Primo, Green, HF-free synthesis of MXene quantum dots and their photocatalytic activity for hydrogen evolution, Small Methods 7 (2023), 2300063.
[11] A.C.Y. Yuen, T.B.Y. Chen, B. Lin, W. Yang, I.I. Kabir, I.M.D.C. Cordeiro, A. E. Whitten, J. Mata, B. Yu, H.-D. Lu, Compos. Part C: Open Access 5 (2021), 100155.
[12] J.I. Kim, J. Kim, J. Lee, D.-R. Jung, H. Kim, H. Choi, S. Lee, S. Byun, S. Kang, B. Park, Effects of crystallization and dopant concentration on the emission behavior of TiO2:Eu nanophosphors, Nanoscale Res. Lett. 7 (2012) 1–7.
[13] L.P.H. Jeurgens, W.G. Sloof, F.D. Tichelaar, E.J. Mittemeijer, Composition and chemical state of the ions of aluminium-oxide films formed by thermal oxidation of aluminium, Surf. Sci. 506 (2002) 313–332.
[14] J. Halim, K.M. Cook, M. Naguib, P. Eklund, Y. Gogotsi, J. Rosen, M.W. Barsoum, X-ray photoelectron spectroscopy of select multi-layered transition metal carbides (MXenes), Appl. Surf. Sci. 362 (2016) 406–417.
[15] J. Zhang, K.A.S. Usman, M.A.N. Judicpa, D. Hegh, P.A. Lynch, J.M. Razal, Applications of X-ray-based characterization in MXene research, Small Methods 7 (2023), 2201527.